

# Production cross-sections and momentum distributions of fragments from neutron-deficient $^{36}\text{Ar}$ at 1.05 A.GeV

M. Caamaño<sup>a</sup>, D. Cortina-Gil<sup>a,b</sup>, K .Sümmerer<sup>b</sup>, J. Benlliure<sup>a</sup>,  
 E. Casarejos<sup>a</sup>, H. Geissel<sup>b</sup>, G. Münzenberg<sup>b</sup>, J. Pereira<sup>a</sup>

<sup>a</sup>*Universidad de Santiago de Compostela, 15706 Santiago de Compostela, Spain*

<sup>b</sup>*Gesellschaft für Schwerionenforschung, Planckstr.1, 64291 Darmstadt, Germany*

---

## Abstract

We have measured production cross sections and longitudinal momentum distributions of fragments from neutron-deficient  $^{36}\text{Ar}$  at 1.05 AGeV. The production cross-sections show excellent agreement with the predictions of the semiempirical formula EPAX. We have compared these results, involving extremely neutron deficient nuclei, with model calculations to extract information about the response of these models close to the driplines. The longitudinal momentum distributions have also been extracted and are compared with the Goldhaber and Morrissey systematics.

*Key words:* Nuclear fragmentation, production cross-sections, fragment longitudinal momentum distributions, geometrical abrasion model, intranuclear-cascades model, semiempirical parameterizations

*PACS:* 25.70.Mn, 25.75-q

---

## 1 Introduction

Projectile fragmentation at high energies ( $\approx 1 A$  GeV) has proven to be a powerful tool to produce clean secondary beams of exotic nuclei that can be used for a wide variety of nuclear-structure, nuclear-reaction, or nuclear-astrophysics studies. To make full use of this potential of projectile fragmentation, the reaction mechanism has to be understood in detail in order to predict precisely the properties of the secondary beams. Pioneering experiments were performed at the LBL Bevalac accelerator [1,2]. Later, more detailed studies have been undertaken at the SIS/FRS exotic beam facility at GSI, Darmstadt

[3,4,5,6]. Comprehensive datasets have been obtained with respect to formation cross sections of exotic fragments as well as their kinematic properties (mainly centroids and widths of longitudinal momentum distributions). Both types of observables could be fitted by empirical parametrizations: the former by the widely used EPAX parametrization [7], the latter by the Morrissey systematics [8]. These parametrizations have turned out to be useful within simulation programs of projectile fragment separators (e.g. MOCADI [9] or LISE [10]). More insight into the underlying physical processes was provided by comparison to physical models like abrasion-ablation (ABRABLA [11,12]) or intranuclear-cascade models (ISABEL [13]).

Since most projectile-fragmentation experiments aim at producing exotic nuclei near the limits of the presently known regions, and since the fragment neutron- or proton-excess is correlated with the neutron- or proton-excess of the projectile [7], fragmentation of stable projectiles outside the valley of  $\beta$ -stability has received most interest. Quite a few studies of neutron-rich projectiles like  $^{48}\text{Ca}$ ,  $^{86}\text{Kr}$ , and  $^{136}\text{Xe}$  have been reported in the literature [2,4,14]. On the proton-rich side, fragmentation cross sections for  $^{58}\text{Ni}$ ,  $^{112}\text{Sn}$ , and  $^{124}\text{Xe}$  have been published [3,15,16]. It was found that the empirical EPAX parametrization could fit the measured cross sections with good accuracy down to sub-nanobarn levels [7].

The present paper aims at complementing the data base for the fragmentation of proton-rich projectiles by studying  $^{36}\text{Ar}$  fragmentation. The isotope  $^{36}\text{Ar}$  is important for producing light proton-rich nuclei at the proton drip line; their properties can be compared to those from  $^{40}\text{Ar}$  fragmentation [1]. In addition to the formation cross sections (down to a level of  $\mu\text{barn}$ ), widths of longitudinal momentum distributions could be measured; both will be compared in the following to the respective systematics as well as to physical model predictions.

## 2 Experimental procedures

The results reported in the present paper were obtained as a by-product of a secondary-reaction experiment aimed at measuring total interaction cross sections of Ar and Cl isotopes [17] as well as measuring longitudinal momentum distributions of knock-out products in coincidence with  $\gamma$ -rays [18]. This is the reason for certain experimental limitations of the present experiment that will be discussed below. The experiment was undertaken at the SIS/FRS facility at GSI in Darmstadt, Germany [19]. SIS delivered a  $^{36}\text{Ar}$  beam with  $1050\text{ A MeV}$  in spills of  $8\text{ s}$  duration with a repetition rate of  $1/16\text{ s}^{-1}$ . Typical beam intensities varied between  $10^8$  and  $10^9$  ions per spill, depending on the cross section to be measured. The primary-beam intensities were measured with

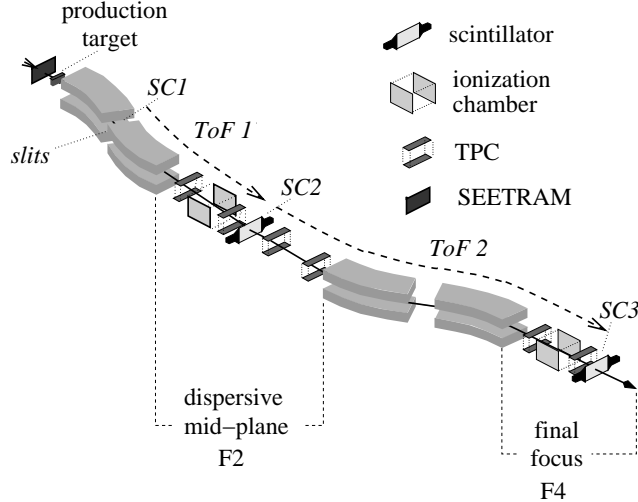


Fig. 1. *A schematic view of the FRagment Separator (FRS) with the detection set-up. The isotope identification was possible in both sections of the spectrometer by measuring the time of flight (TOF) between scintillators (SC) and the energy deposition in ionization chambers. Several position-sensitive detectors (TPC) allowed tracking of projectiles and fragments and momentum measurements of the fragments.*

a secondary-electron transmission monitor (SEETRAM) [20] that was calibrated with respect to a fast scintillator detector. Fragments were produced in a thick ( $1625 \text{ mg/cm}^2$ )  ${}^9\text{Be}$  target located at the entrance of the FRS.

Fragments were identified with respect to their nuclear charge,  $Z$ , and their mass-over-charge ratio,  $A/Z$ , by a combination of energy-deposition, magnetic rigidity and time-of-flight (ToF) measurements. The set-up used is shown in Fig.1. While in principle both observables can be measured in both sections of the FRS, only the first half up to F2 was used to identify and count the fragments. To this end, the energy deposition in an ionization chamber at F2 was measured together with the time of flight (ToF1) between scintillators “SC1” and “SC2”. Positions and angles at F2 could be determined with the help of two position-sensitive detectors (TPC). The ToF was calibrated with the primary  ${}^{36}\text{Ar}$  beam from SIS with several known energies which allowed to determine the length of the flight path and the offset. Together with magnetic rigidity ( $B\rho$ ) determined from Hall-probe measurements and corrections for deviations from the optical axis, the ToF gave  $A/Z$  of the fragments. At the same time, the velocity-dependent energy deposition of the beam was recorded and calibrated in terms of nuclear charge,  $Z$ . Typical results of the isotope identification obtained are visualized in Fig.2. The non-observation of the unbound nuclei  ${}^{19}\text{Na}$  and  ${}^{16}\text{F}$  allowed to verify independently the isotope identification.

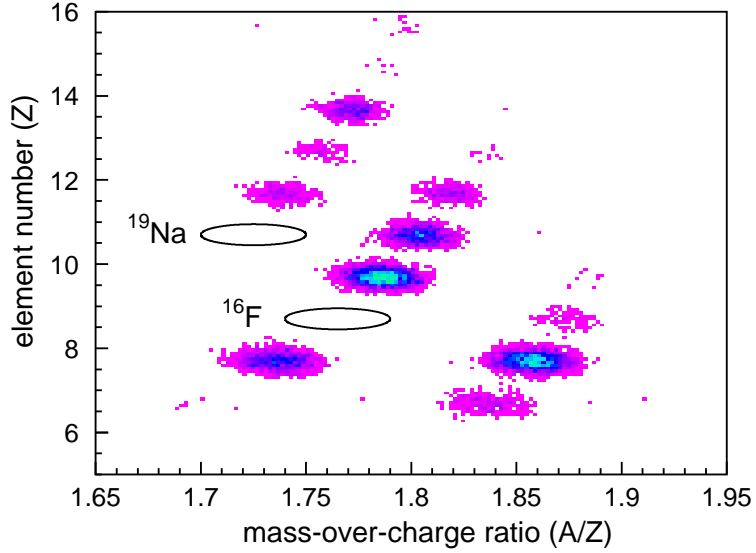


Fig. 2. An example of the fragment identification in the first half of the FRS. The isotope identification is confirmed by the non-observation of the unbound nuclei  $^{19}\text{Na}$  and  $^{16}\text{F}$ .

### 3 Data analysis and results

In the present experiment, the requirements of the main secondary-reaction study dictated an experimental setup that was not optimum for the present purpose. The main limitation was the width of the F1 start scintillator (“SC1” in Fig.1) of only 2 cm in x- (bending) direction. This leads to important cuts in the fragment longitudinal momentum distributions such that several  $B\rho$  settings had to be analyzed to cover the entire phase space distribution of each fragment. Each  $B\rho$  setting allowed to produce a two-dimensional spectrum as the one shown in Fig.2. For each isotope selected by a two-dimensional condition in Fig.2, its x-distribution in the F2 momentum-dispersive focal plane was converted to a longitudinal momentum distribution and properly normalized with the help of the SEETRAM beam current detector. The reconstructed magnetic rigidity distribution of the isotope  $^{14}\text{O}$  is shown in Fig.3.

The reconstructed Gaussians for each isotope yield directly the average longitudinal momentum in the laboratory frame and the momentum width. From their areas, production cross sections can be determined once the necessary corrections have been applied.

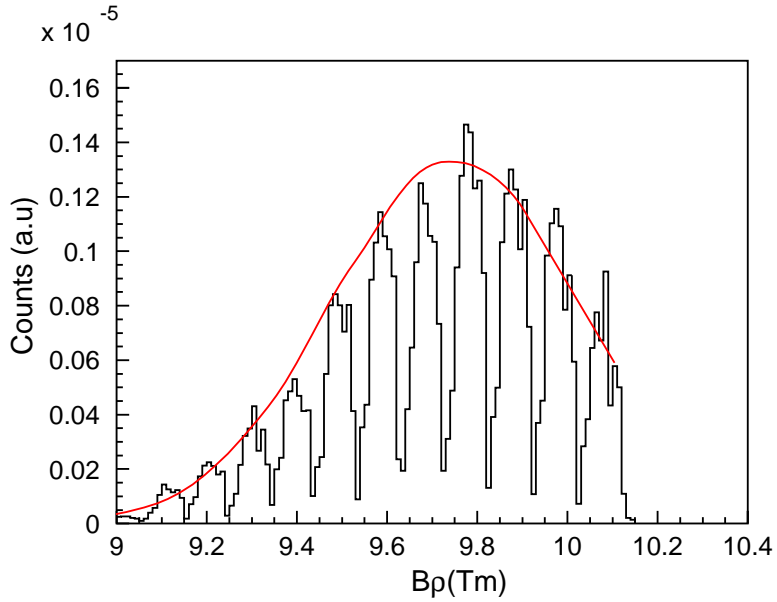


Fig. 3. Magnetic-rigidity distribution of the fragment  $^{14}\text{O}$  reconstructed from several normalized  $B\rho$  settings. The envelope of the distribution is fitted to a Gaussian.

### 3.1 Production cross-sections

An important ingredient in determining the production cross sections is the transmission calculation. In bending direction, a  $B\rho$  scan allows to cover the entire longitudinal momentum distribution of each fragment or at least to cover enough momentum space that a Gaussian fit to the data is possible. The same is not possible, however, perpendicular to the bending plane. This means that the angular acceptance for each isotope has to be calculated numerically, based on its measured longitudinal momentum width and assuming that longitudinal and transverse momentum widths are identical. The numerical procedures have been published in Ref. [21]. It is well known that the momentum widths depend approximately on the square root of the mass difference between projectile and fragment (e.g. Ref. [8]). Consequently, the transmission of fragments close to the  $^{36}\text{Ar}$  projectile (like the Ar or Cl fragments in Table 1) are transmitted with about 100%, whereas the isotopes  $^{12,13}\text{N}$  are transmitted only with about 33% efficiency.

Further corrections to the isotope yields are due to the dead time of the data acquisition (approximately between 50% and 70%) and secondary reactions of the produced residues in the target (of about 10%). Finally, the observed number of counts of each isotope is converted to a cross section using the number of target atoms and the number of incident ions as determined from the SEETRAM beam intensity monitor. The resulting production cross sections for 38 isotopes are listed in Table 1 and visualized in Fig.4.

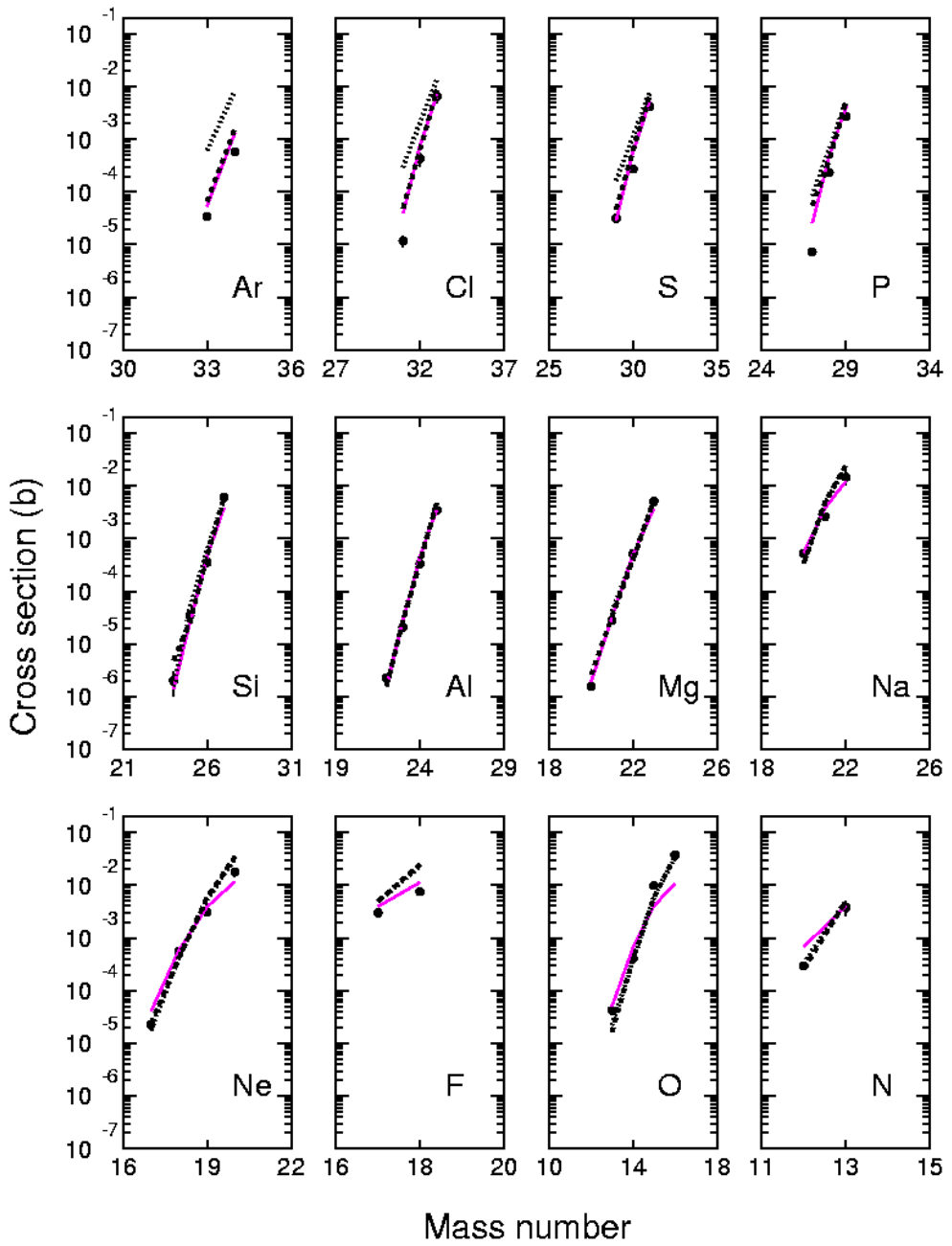


Fig. 4. Production cross sections of neutron-deficient  $^{36}\text{Ar}$  fragments measured at 1050 A MeV. Solid lines link EPAX [7] predictions. Dotted and dashed lines depict model calculations with the ISABEL intranuclear- cascade [13] and the ABRABLA abrasion-ablation model [11], respectively.

Table 1

*Production cross sections of neutron-deficient fragments from  $^{36}\text{Ar}$  measured at 1050 A MeV*

Isotope	$\sigma_{prod}$ (b)	Isotope	$\sigma_{prod}$ (b)
$^{12}\text{N}$	$(2.97 \pm 0.09) \cdot 10^{-4}$	$^{22}\text{Al}$	$(2.30 \pm 0.30) \cdot 10^{-6}$
$^{13}\text{N}$	$(3.72 \pm 1.19) \cdot 10^{-3}$	$^{23}\text{Al}$	$(2.10 \pm 0.30) \cdot 10^{-5}$
$^{13}\text{O}$	$(4.20 \pm 0.20) \cdot 10^{-5}$	$^{24}\text{Al}$	$(3.34 \pm 0.13) \cdot 10^{-4}$
$^{14}\text{O}$	$(4.12 \pm 0.13) \cdot 10^{-4}$	$^{25}\text{Al}$	$(3.48 \pm 0.52) \cdot 10^{-3}$
$^{15}\text{O}$	$(9.82 \pm 0.29) \cdot 10^{-3}$	$^{24}\text{Si}$	$(2.00 \pm 1.00) \cdot 10^{-6}$
$^{16}\text{O}$	$(3.76 \pm 0.64) \cdot 10^{-2}$	$^{25}\text{Si}$	$(3.40 \pm 0.10) \cdot 10^{-5}$
$^{17}\text{F}$	$(2.99 \pm 0.09) \cdot 10^{-3}$	$^{26}\text{Si}$	$(3.52 \pm 0.11) \cdot 10^{-4}$
$^{18}\text{F}$	$(7.58 \pm 1.35) \cdot 10^{-3}$	$^{27}\text{Si}$	$(6.13 \pm 1.04) \cdot 10^{-3}$
$^{17}\text{Ne}$	$(2.30 \pm 0.10) \cdot 10^{-5}$	$^{27}\text{P}$	$(7.40 \pm 1.40) \cdot 10^{-6}$
$^{18}\text{Ne}$	$(5.67 \pm 0.17) \cdot 10^{-4}$	$^{28}\text{P}$	$(2.33 \pm 0.09) \cdot 10^{-4}$
$^{19}\text{Ne}$	$(3.12 \pm 0.09) \cdot 10^{-3}$	$^{29}\text{P}$	$(2.78 \pm 0.17) \cdot 10^{-3}$
$^{20}\text{Ne}$	$(1.80 \pm 0.40) \cdot 10^{-2}$	$^{29}\text{S}$	$(3.20 \pm 0.10) \cdot 10^{-5}$
$^{20}\text{Na}$	$(5.24 \pm 0.15) \cdot 10^{-4}$	$^{30}\text{S}$	$(2.73 \pm 0.11) \cdot 10^{-4}$
$^{21}\text{Na}$	$(2.63 \pm 0.38) \cdot 10^{-3}$	$^{31}\text{S}$	$(4.17 \pm 0.39) \cdot 10^{-3}$
$^{22}\text{Na}$	$(1.47 \pm 0.46) \cdot 10^{-2}$	$^{31}\text{Cl}$	$(1.20 \pm 0.30) \cdot 10^{-5}$
$^{20}\text{Mg}$	$(1.60 \pm 0.30) \cdot 10^{-6}$	$^{32}\text{Cl}$	$(4.36 \pm 1.32) \cdot 10^{-4}$
$^{21}\text{Mg}$	$(2.80 \pm 0.50) \cdot 10^{-5}$	$^{33}\text{Cl}$	$(6.59 \pm 1.87) \cdot 10^{-3}$
$^{22}\text{Mg}$	$(5.19 \pm 0.21) \cdot 10^{-4}$	$^{33}\text{Ar}$	$(3.40 \pm 0.10) \cdot 10^{-5}$
$^{23}\text{Mg}$	$(5.13 \pm 0.15) \cdot 10^{-3}$	$^{34}\text{Ar}$	$(5.73 \pm 0.19) \cdot 10^{-4}$

The errors involved in the cross section determination are partly constant (2% each for the angular acceptance determination [21] and beam intensity determination) and partly vary appreciably from isotope to isotope. The main contribution comes from the errors of the Gaussian fit to the reconstructed momentum distributions. The total combined errors of the production cross sections vary between 3% and about 30% with the exception of  $^{24}\text{Si}$  where the error is about 50%.

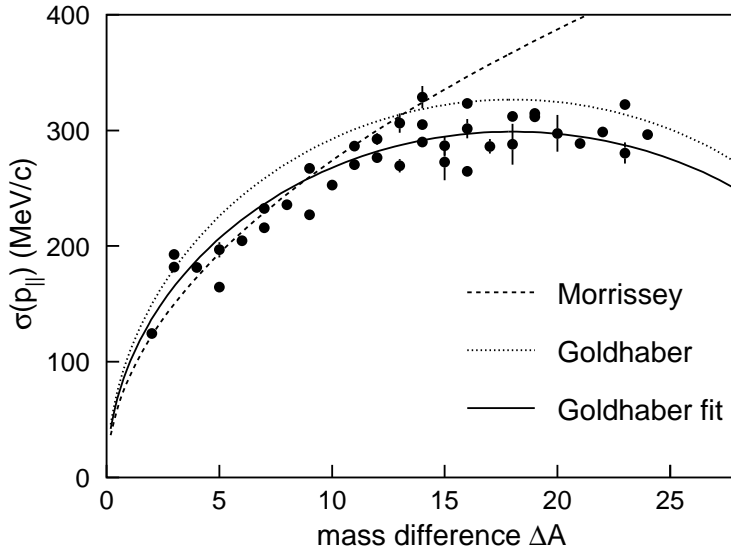


Fig. 5. Widths of the longitudinal momentum distributions plotted as a function of mass loss,  $\Delta A$ , from the projectile. The dashed curve shows the  $\sqrt{\Delta A}$  dependence of the Morrissey systematics [8]. The dotted curve follows Goldhaber's model [25]. The full curve has been obtained by fitting the constant  $\sigma_0$  in Goldhaber's model to the present data (see text).

### 3.2 Momentum distributions

As mentioned earlier, the momentum distributions for each isotope result directly from Gaussian fits to the reconstructed  $B\rho$  distributions such as the one shown in Fig. 3. The resulting laboratory momenta are then transformed to the projectile system. As it is well known, the centroid values are small (on the order of 100-200 MeV/c), i.e. the fragments have practically the same velocity as the projectile beam. The central momenta decrease approximately linearly with mass loss from the projectile, with a slope similar to what can be found in the Morrissey systematics [8]. Since the error bars in our measurements are rather large, and do not give more insight than what can be found in the literature, we do not discuss this observable here.

The widths of the longitudinal momentum distributions,  $\sigma(p_{||})$ , are listed in Table 2 and are shown graphically in Fig. 5. A marked deviation from the parabolic shape predicted by the Morrissey systematics [8] is clearly visible above a mass difference of 10 units between fragment and projectile.

Table 2

*Longitudinal momentum widths in the projectile system of neutron-deficient fragments from  $^{36}\text{Ar}$  measured at 1050 A MeV*

Isotope	$\sigma(p_{  })$ (MeV/c)	Isotope	$\sigma(p_{  })$ (MeV/c)
$^{12}\text{N}$	$296 \pm 2$	$^{23}\text{Al}$	$269 \pm 6$
$^{13}\text{N}$	$322 \pm 3$	$^{23}\text{Mg}$	$306 \pm 8$
$^{13}\text{O}$	$281 \pm 10$	$^{24}\text{Al}$	$293 \pm 5$
$^{14}\text{O}$	$299 \pm 1$	$^{24}\text{Si}$	$277 \pm 4$
$^{15}\text{O}$	$289 \pm 4$	$^{25}\text{Al}$	$286 \pm 2$
$^{16}\text{O}$	$297 \pm 16$	$^{25}\text{Si}$	$270 \pm 3$
$^{17}\text{F}$	$315 \pm 4$	$^{26}\text{Si}$	$253 \pm 2$
$^{17}\text{Ne}$	$312 \pm 3$	$^{27}\text{P}$	$227 \pm 4$
$^{18}\text{F}$	$288 \pm 18$	$^{27}\text{Si}$	$267 \pm 3$
$^{18}\text{Ne}$	$312 \pm 3$	$^{28}\text{P}$	$236 \pm 3$
$^{19}\text{Ne}$	$286 \pm 6$	$^{29}\text{P}$	$216 \pm 2$
$^{20}\text{Mg}$	$265 \pm 4$	$^{29}\text{S}$	$233 \pm 2$
$^{20}\text{Na}$	$323 \pm 4$	$^{30}\text{S}$	$205 \pm 2$
$^{20}\text{Ne}$	$302 \pm 8$	$^{31}\text{Cl}$	$165 \pm 2$
$^{21}\text{Mg}$	$287 \pm 8$	$^{31}\text{S}$	$197 \pm 7$
$^{21}\text{Na}$	$273 \pm 16$	$^{32}\text{Cl}$	$182 \pm 3$
$^{22}\text{Al}$	$290 \pm 1$	$^{33}\text{Ar}$	$182 \pm 4$
$^{22}\text{Mg}$	$305 \pm 4$	$^{33}\text{Cl}$	$193 \pm 2$
$^{22}\text{Na}$	$329 \pm 10$	$^{34}\text{Ar}$	$124 \pm 3$

## 4 Discussion

### 4.1 Production cross- sections

The present data constitute an excellent data base to benchmark the predictive power of different fragmentation models at the limit of unbound nuclei. At these energies, the fragmentation process is described in terms of a two-step model. In the first step, the collision between the nucleons in the overlap region between projectile and target leads to the formation of two residues of both reaction partners called prefragments, with similar kinematical prop-

erties, smaller mass and a given excitation energy. In the second step, the residues of both reaction partners release their energy excess by evaporating nucleons and  $\gamma$ -rays. The proximity of the investigated nuclei to the proton drip line is expected to increase the sensitivity of their production cross sections to the excitation energy induced in the first stage of the collision or the competition between proton and neutron evaporation during the second stage.

To investigate the reaction mechanism leading to the formation of the measured nuclei we have performed calculations using two different models to describe the first stage of the reaction, the intranuclear-cascade model ISABEL [13] and the abrasion model of Gaimard and Schmidt [11]. Both models were coupled to the ABLA evaporation code [12] to describe the second stage of the reaction. These two models follow completely different approaches. In the intranuclear-cascade model ISABEL, the interaction between projectile and target is described as a sequence of elastic or inelastic nucleon-nucleon collisions. The moving nucleons follow classical trajectories and the only quantum mechanical ingredient is the Pauli blocking. Nucleons with sufficiently high momenta can leave their respective nuclear volumes, the leftover nucleons form the prefragment. The final prefragment excitation energy is obtained from particle-hole excitations in the initial Fermi distribution of the removed nucleons plus the energies of the scattered nucleons that end up below the “cutoff energy”; the latter has been introduced to terminate the history of cascade nucleons with energies too low to escape their respective potential wells [13].

The abrasion model follows geometrical considerations, the size of the projectile and target prefragments is given by the non-overlapping region between both partners, which is defined by the impact parameter. The excitation energy induced in the collision is determined by the energy of the holes of the removed nucleons, assuming a Fermi distribution of nucleons inside the nucleus, which has been empirically demonstrated to be on average around 27 MeV per abraded nucleon [22].

Other than the physical models discussed above, the empirical parametrization of fragmentation cross sections, EPAX [7], has little physical input and merely aims at reproducing measured data by numerical expressions. Such an approach is nevertheless useful e.g. for planning experiments or for cases where fast iterative calculations of secondary cross sections are needed. In the present context, the EPAX formula is particularly useful since it contains a parametrization of the “memory effect”, i.e. the influence of the proton excess of the projectile on the proton excess of the fragments. As explained in detail in Ref. [7], the numerical form of this “memory effect” has been adjusted to measured  $^{58}\text{Ni}$  fragmentation cross sections. A comparison with the present high-precision  $^{36}\text{Ar}$  cross sections can serve as a check of the predictive power of EPAX for proton-rich projectiles.

In figure 4 we compare the measured production cross sections with the results of the calculations obtained with the intranuclear-cascade model ISABEL (dotted lines) and the abrasion model of Gaimard and Schmidt ABRA (dashed lines) coupled with the ABLA evaporation model. The predictions obtained with the semi-empirical parametrization EPAX are included in this figure as well (solid line) .

In general the three calculations provide a very good description of the measured cross sections even for weakly bound nuclei at the proton drip line. Only a detailed comparison shows some trends. The ISABEL calculation seems to overestimate the production cross sections of heavy-projectile residues while the abrasion model provides an excellent description of all the data. Since both calculations use the same evaporation model the observed deviations must be due to the different models used to describe the first stage of the collision. In addition, residues close to the projectile do not reach the limiting fragmentation regime and consequently their production cross section is sensitive to the entrance channel. The observed overestimation of the production cross section with ISABEL can be explained if one considers that this code produces fragments with 20% less excitation energy on average than the ABRA code. As pointed out, the production of heavy projectile residues is very much affected by the first stage of the collision. In particular, a lower excitation energy leads to shorter evaporation chains and consequently an increase of the production cross section of heavy residues. The good description of these data with the abrasion-ablation model ABRABLA confirms its predictive power and validates the physical assumptions used in this code.

The overall agreement of the measured production cross sections with the EPAX formula [7] is excellent, as can be seen in Fig.4. The present experiment reaches the proton drip line up to  $Z = 13$ , Al. Even drip-line nuclei are produced with cross sections that lie well on the EPAX predictions. This confirms observations that were made for another neutron-deficient projectile,  $^{58}\text{Ni}$  [3].

Our new data for  $^{36}\text{Ar}$  ( $N/Z = 1.0$ ) allow to test the EPAX predictions for the production of exotic nuclei over a wide range of projectile- $N/Z$  values by comparing them to similar data from  $^{43}\text{Ar}$  ( $N/Z = 2.39$ ) on  $^{12}\text{C}$  at 222  $A$  MeV [23]. We assume that for both incident energies, 222 and 1050 AMeV, the cross sections are largely energy-independent, so that EPAX can be applied. Fig. 6 demonstrates that at least the proton-rich slopes of the  $^{36}\text{Ar}$ -induced distributions and the neutron-rich slopes of the  $^{43}\text{Ar}$ -induced distributions are correctly predicted by EPAX. Similarly good agreement was found for isotope distributions from  $^{96}\text{Ru}$  and  $^{96}\text{Zr}$  fragmentation [24].

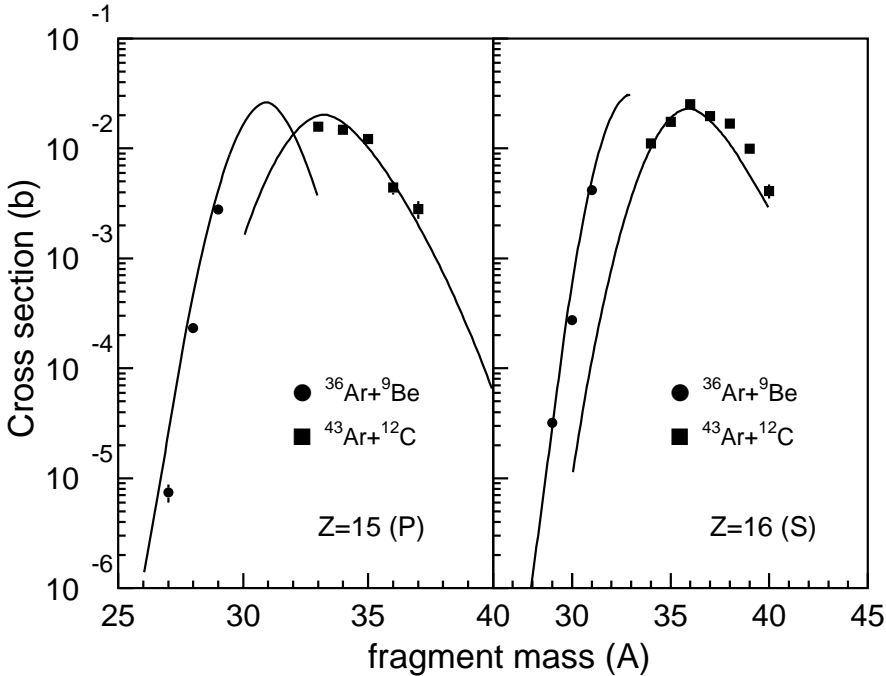


Fig. 6. Production cross sections of  $P$  isotopes (left) and  $S$  isotopes (right) from the fragmentation of  $^{36}\text{Ar} + ^9\text{Be}$  at  $1050 \text{ A MeV}$  (circles, this work) in comparison to data from  $^{43}\text{Ar} + ^{12}\text{C}$  fragmentation at  $222 \text{ A MeV}$  (squares, Ref. [23]). The curves denote the respective EPAX predictions.

#### 4.2 Momentum distributions

A precise knowledge of the kinematics of high-energy projectile fragmentation is essential to correctly predict the yields of secondary beams from an in-flight separator like the FRS. We have discussed in subsect. 3.1 how the transmission of the FRS is affected by the momentum distributions.

In the traditional two-step model of high-energy projectile fragmentation, the momentum widths are largely determined by the random addition of the Fermi momenta of the nucleons that are knocked out in the first (“abrasion”) phase of the reaction. The corresponding prefragment momentum widths have been given by Goldhaber [25] as

$$\sigma(p_{||}) = \sigma_0 \sqrt{\frac{A_{pf}(A_p - A_{pf})}{A_p - 1}} = \frac{p_F}{\sqrt{5}} \sqrt{\frac{A_{pf}(A_p - A_{pf})}{A_p - 1}} \quad (1)$$

where  $A_p(A_{pf})$  refers to the projectile (prefragment) mass; the latter cannot be observed. The quantity  $p_F$  denotes the Fermi momentum of the nucleons in the projectile. Subsequent evaporation (“ablation”) of nucleons in the sec-

ond phase additionally broadens the momentum distributions somewhat, but the most important effect here is that the number of nucleons is reduced, so that the original “Goldhaber” distribution becomes flatter and can be better described (at least for fragments close to the projectile mass) by Morrissey’s formula [8]:

$$\sigma(p_{||}) = \frac{150}{\sqrt{3}} \sqrt{A_p - A_f} \quad (2)$$

where now  $A_f$  denotes the (observed) fragment mass. Systematic studies of the validity of the Morrissey systematics have been undertaken about a decade ago at the FRS (e.g. Ref. [26]).

Up to about a mass loss of 10 units, the present data follow nicely the Morrissey systematics (dashed curve in Fig. 5). For fragments further removed from the projectile, however, the widths tend to saturate. Similar observations were made in a comprehensive study of  $^{86}\text{Kr}$  fragmentation at 500  $A$  MeV [4], where it was found that the widths even became smaller again for fragments with masses smaller than about half the projectile mass. One practical solution is to keep the Goldhaber formula (Eq. 1) but fit the width coefficient  $\sigma_0$  to the measured data of Fig. 6 (full line). This leads to a parameter of  $\sigma_0^f = 98.2 \pm 0.2$  MeV/c, smaller than the Goldhaber prediction (for *prefragments*) of  $\sigma_0^{pf} = 112$  MeV/c. The latter value is based on a Fermi momentum in  $^{36}\text{Ar}$  of  $p_F = 250$  MeV/c [27]. The smaller  $\sigma_0^f$  value reflects the evaporation mass loss as discussed above. It compares well with other data found in the literature for light nuclei, e.g. Viyogi *et al.* (Ref. [1]) found  $\sigma_0 = 94 \pm 5$  MeV/c for  $^{40}\text{Ar}$  at 213 AMeV.

## 5 Summary

We have studied the fragmentation of neutron-deficient  $^{36}\text{Ar}$  at relativistic energies and have obtained precise values for production cross sections and longitudinal momentum widths of very neutron-deficient fragments, reaching the proton-drip line up to aluminum. Both observables can be reproduced well by their respective empirical parametrizations: the cross sections match excellently those predicted by the EPAX formula, thus confirming its validity also for the case of very neutron-deficient projectiles. The longitudinal momentum widths are best fitted by a modified Goldhaber formula, where the width constant  $\sigma_0$  is replaced by an empirical value. The measured production cross sections are also compared with physical-model calculations performed with (i) the ISABEL intranuclear-cascade model, and (ii) the Gaimard-Schmidt abrasion model, both coupled to a standard evaporation code (ABLA). The

ISABEL code gives an overall good description of the data however, some discrepancies are observed for the heavier residues. For these nuclides very close to the projectile the ISABEL code clearly overestimate the production cross sections. This result is interpreted as a consequence of an underestimation of the excitation energy induced in the reaction; lower excitation energies lead to shorter evaporation chains which increase the production of residues close to the projectile. The abrasion model ABRABLA provide an extremely good description of all the data.

These results indicate that in the range of fragment masses studied here the assumption of a two-stage model works well; the model consists of a fast removal of quasi-free nucleons during the geometrical overlap of projectile and target, followed by evaporation of particles from a thermally equilibrated prefragment. In addition, we confirm the predictive power of the abrasion code that can also be used to describe the production of residual nuclides in more complex reactions where the EPAX formula can not be applied, as it is the case for fissile projectiles.

## 6 Acknowledgements

The authors wish to express their gratitude to their colleagues from the accompanying experiments for their help with the experimental setup. They also acknowledge technical support from A. Brünle, K.H. Behr, and K. Burkard. This work was supported by the EU under contract ERBFMECT95 0083, and by the Spanish Ministry of Science and Technology under contract number FPA2001-0144-C05-4-01.

## References

- [1] Y.P. Viyogi, T.J.M. Symons, P. Doll, D.E. Greiner, H.H. Heckman, D.L. Hendrie, P.J. Lindstrom, J. Mahoney, D.K. Scott, K. Van Bibber, G.D. Westfall, H. Wieman, H.J. Crawford, C. McParland, C.K. Gelbke, Phys. Rev. Lett. **42** (1979) 33.
- [2] G.D. Westfall, T.J. M.Symons, D.E. Greiner, H.H. Heckman, P.J. Lindstrom, J. Mahoney, A.C. Shotter, D.K. Scott, H.J. Crawford, C. McParland, T.C. Awes, C.K. Gelbke, J.M.Kidd, Phys. Rev. Lett. **43** (1979) 1859.
- [3] B. Blank, S. Andriamonje, R. Del Moral, J.P. Dufour, A. Fleury, T. Joso, M.S. Pravikoff, S. Czajkowski, Z. Janas, A. Piechaczek, E. Roeckl, K.-H. Schmidt, K. Sümmerer, W. Trinder, M. Weber, T. Brohm, A. Grewe, E. Hanelt, A. Heinz, A. Junghans, C. Rohl, S. Steinhäuser, B. Voss, M. Pfützner, Phys. Rev. C **50**(1994) 2398.

- [4] M. Weber, C. Donzaud, J.P. Dufour, H. Geissel, A. Grewe, D. Guillemaud-Mueller, H. Keller, M. Lewitowicz, A. Magel, A.C. Mueller, G. Münzenberg, F. Nickel, M. Pfützner, A. Piechaczek, M. Pravikoff, E. Roeckl, K. Rykaczewski, M.G. Saint-Laurent, I. Schall, C. Stephan, K. Sümmerer, L. Tassan-Got, D.J. Vieira, B. Voss, Nucl. Phys. A **578** (1994) 659.
- [5] J. Reinhold, J. Friese, H.-J. Körner, R. Schneider, K. Zeitelhack, H. Geissel, A. Magel, G. Münzenberg, K. Sümmerer, Phys. Rev. C **58** (1998) 247.
- [6] M. de Jong, K.-H. Schmidt, B. Blank, C. Böckstiegel, T. Brohm, H.-G. Clerc, S. Czajkowski, M. Dornik, H. Geissel, A. Grewe, E. Hanelt, A. Heinz, H. Irnich, A.R. Junghans, A. Magel, G. Münzenberg, F. Nickel, M. Pfützner, A. Piechaczek, C. Scheidenberger, W. Schwab, S. Steinhäuser, K. Sümmerer, W. Trinder, B. Voss, C. Ziegler, Nucl. Phys. A **628** (1998) 479.
- [7] K. Sümmerer and B. Blank, Phys. Rev. C **61** (2000) 034607.
- [8] D.J. Morrissey, Phys. Rev. C **39** (1989) 460.
- [9] N. Iwasa, H. Geissel, G. Münzenberg, C. Scheidenberger, T. Schwab, H. Wollnik, Nucl. Instr. Meth. Phys. Res. B **126** (1997) 284.
- [10] D. Bazin, M. Lewitowicz, O. Sorlin, O. Tarasov, Nucl. Instr. Meth. Phys. Res. A **482** (2002) 314.
- [11] J.-J. Gaimard and K.-H Schmidt, Nucl. Phys. A **531** (1991) 709.
- [12] A.R. Junghans, M. de Jong, H.-G. Clerc, A.V. Ignatyuk, G.A. Kudyaev, K.-H. Schmidt, Nucl. Phys. A **629** (1998) 635.
- [13] Y. Yariv and Z. Fraenkel, Phys. Rev. C **20** (1979) 2227.
- [14] J. Friese, H.-J. Körner, J. Reinhold, R. Schneider, H. Trieb, K. Zeitelhack, B. Blank, T. Brohm, Y. Fujita, H. Geissel, W. Konig, G. Münzenberg, F. Nickel, M. Pfützner, K. Rykaczewski, I. Schall, D. Schardt, A. Schröter, M. Steiner, K. Sümmerer, B. Voss, J. Weckenmann, Nucl. Phys. A **553** (1993) 753c.
- [15] A. Stolz, T. Faestermann, J. Friese, P. Kienle, H.-J. Körner, M. Münch, R. Schneider, E. Wefers, K. Zeitelhack, K. Sümmerer, H. Geissel, J. Gerl, G. Münzenberg, C. Schlegel, R.S. Simon, H. Weick, M. Hellström, M.N. Mineva, P. Thirolf, Phys. Rev. C **65** (2002) 064603.
- [16] R. Schneider, J. Friese, J. Reinhold, K. Zeitelhack, T. Faestermann, R. Gernhauser, H. Gilg, F. Heine, J. Homolka, P. Kienle, H.J. Körner, H. Geissel, G. Münzenberg, K. Sümmerer, Z. Physik A **348** (1994) 241.
- [17] A. Ozawa, T. Baumann, L. Chulkov, D. Cortina, U. Datta, J. Fernandez, H. Geissel, F. Hammache, K. Itahashi, M. Ivanov, R. Janik, T. Kato, K. Kimura, T. Kobayashi, K. Markenroth, M. Meister, G. Münzenberg, T. Ohtsubo, S. Ohya, T. Okuda, A.A. Ogloblin, V. Pribora, M. Sekiguchi, B. Sitar, P. Strmen, S. Sugimoto, K. Sümmerer, T. Suzuki, I. Tanihata, Y. Yamaguchi, Nucl. Phys. A **709** (2002) 60.

- [18] D. Cortina-Gil, J. Fernandez-Vazquez, F. Attallah, T. Baumann, J. Benlliure, M.J.G. Borge, L. Chulkov, C. Forssen, L.M. Fraile, H. Geissel, J. Gerl, K. Itahashi, R. Janik, B. Jonson, S. Mandal, K. Markenroth, M. Meister, M. Mocko, G. Münzenberg, T. Ohtsubo, A. Ozawa, V. Pribora, K. Riisager, R. Schneider, H. Scheit, G. Schrieder, H. Simon, B. Sitar, A. Stolz, P. Strmen, K. Sümmmerer, I. Szarka, S. Wan, H. Weick, in preparation.
- [19] H. Geissel, P. Armbruster, K.-H. Behr, A. Brünle, K. Burkard, M. Chen, H. Folger, B. Franczak, H. Keller, O. Klepper, B. Langenbeck, F. Nickel, E. Pfeng, M. Pfützner, E. Roeckl, K. Rykaczewski, I. Schall, D. Schardt, C. Scheidenberger, K.-H. Schmidt, A. Schröter, T. Schwab, K. Sümmmerer, M. Weber, G. Münzenberg, T. Brohm, H.-G. Clerc, M. Fauerbach, J.-J. Gaimard, A. Grewe, E. Hanelt, B. Knödler, M. Steiner, B. Voss, J. Weckenmann, C. Ziegler, A. Magel, H. Wollnik, J.P. Dufour, Y. Fujita, D.J. Viera, B. Sherrill, Nucl. Instr. and Methods B **70** (1992) 286.
- [20] B. Jurado, K.-H. Schmidt, K.-H. Behr, Nucl. Instr. Meth. Phys. Res. A **483** (2002) 603.
- [21] J. Benlliure, J. Pereira-Conca, and K.-H. Schmidt, Nucl. Instr. Meth. Phys. Res. A **478** (2002) 493.
- [22] K.-H. Schmidt, A. Heinz, H.-G. Clerc, B. Blank, T. Brohm, S. Czajkowski, C. Donzaud, H. Geissel, E. Hanelt, H. Irnich, M.C. Itkis, M. de Jong, A. Junghans, A. Magel, G. Münzenberg, F. Nickel, M. Pfützner, A. Piechaczek, C. Rohl, C. Scheidenberger, W. Schwab, S. Steinhäuser, K. Sümmmerer, W. Trinder, B. Voss, S.V. Zhdanov , Phys. Lett. B **300** (1993) 313.
- [23] Shuying Wan , Ph.D. Thesis, University of Heidelberg (1999).
- [24] K. Sümmmerer and B. Blank, Nucl. Phys. A **701** (2000) 161c.
- [25] A.S. Goldhaber, Phys. Lett. B **53** (1974) 244.
- [26] E. Hanelt, A. Grewe, K.-H. Schmidt, T. Brohm, H.-G. Clerc, M. Dornik, M. Fauerbach, H. Geissel, A. Magel, G. Münzenberg, F. Nickel, M. Pfützner, C. Scheidenberger, M. Steiner, K. Sümmmerer, B. Voss, M. Weber, J. Weckenmann, C. Ziegler, Z. Physik A **346** (1993) 43.
- [27] E.J. Moniz, I. Sick, R.R. Whitney, J.R. Ficenec, R.D. Kephart, W.P. Trower , Phys. Rev. Lett. **26** (1971) 445.